

The Temporal Optical Behavior of the Hubble Space Telescope: The Impact on Science Observations

Russell B. Makidon^a, Matthew D. Lallo^a, Stefano Casertano^a, Ronald L. Gilliland^a,
Marco Sirianni^a, & John E. Krist^b

^aSpace Telescope Science Institute, 3700 San Martin Drive, Baltimore, MD, 21218, USA;

^bJet Propulsion Laboratory, 4800 Oak Grove Drive, Pasadena, CA 91109, USA

ABSTRACT

Though the Hubble Space Telescope (HST) has proven to be a stable platform for astronomical observations when compared with ground-based imaging, it features its own characteristic optical variations that have required post-observation processing to support the full range of science investigations that should be possible with HST. While the overall system focus has been monitored and adjusted throughout the life of the Observatory, the recent installation of the Advanced Camera for Surveys and its High Resolution Camera has allowed us to use phase retrieval techniques to accurately measure changes in coma and astigmatism as well. The aim of this current work is to relate these measurements of wave front error back to characterizations more common to science data analysis (e.g. FWHM, and ellipticity). We show how variations in these quantities over the timescales observed may impact the photometric and astrometric precision required of many current HST programs, as well as the characterization of barely-resolved objects. We discuss how improved characterization and modeling of the point spread function (PSF) variations may help HST observers achieve the full science capabilities of the Observatory.

Keywords: Hubble Space Telescope, Point Spread Functions, optical observations, temporal variations

1. INTRODUCTION

The Hubble Space Telescope (HST) is, by any measure, one of the most productive scientific facilities in history. Launched on-board the shuttle Discovery (STS-31) April 24, 1990 and released into low-Earth orbit on April 26, 1990, early science with the HST was marred by an improperly-figured primary mirror that produced 0.5 waves RMS of spherical aberration at the focal plane at a wavelength of $\lambda = 0.50\mu\text{m}$. In spite of this, the relative sensitivity and stability of HST as an observational platform enabled discoveries that were unavailable from ground-based observatories.¹⁻³

Designed as a serviceable and upgradeable platform, HST has been the focus of four Servicing Missions since launch (1993, 1997, 1999 and 2002). Each of these Servicing Missions has provided significant upgrades to HST's hardware and suite of scientific instruments. Notable among these upgrades has been the installation of two generations of solar panels, a suite of gyroscopes, and four new science instruments - the Wide Field Planetary Camera 2 (WFPC2), the Near Infrared Camera and Multi-Object Spectrometer (NICMOS), the Space Telescope Imaging Spectrometer (STIS), and the Advanced Camera for Surveys (ACS), each with internal optics to correct for HST's spherically aberrated Primary Mirror. These changes have resulted in an observatory that is currently more stable and more sensitive than at any time in its history, enabling HST to continue to produce cutting-edge science more than sixteen years after its launch.

Despite these improvements to HST's stability and imaging quality, many observers still face unique challenges when trying to push to the limits of their scientific observations. High contrast imaging, the detection and characterization of weak gravitational lens systems, crowded-field stellar photometry, and ultra-precise astrometry are just a few examples of science that is challenged by small variations in the HST point spread function (PSF). In a companion work,⁴ we present some of the unique behavior of the temporal variations of the HST PSF, while in this work we outline how these challenges impact science observations like those mentioned above.

Further author information: (Send correspondence to R.B.M.: E-mail: makidon@stsci.edu)

2. THE NATURE OF HST’S OPTICAL QUALITY

It has been known since early in the HST mission that the Observatory’s focal length varies on both orbital and longer time scales. These changes have generally been attributed to the physical motion of the Secondary Mirror (SM) relative to the Primary Mirror (PM), most likely resulting from variations in the metering truss structure that supports the SM. Successive improvements in the complement of instruments aboard HST have generally increased the sensitivity of image quality to focus, improving our ability to measure the focus and infer the SM position through the properties of the observed PSF.⁴

While many HST observing programs are not critically dependent on the stability of the HST PSF, an increasing number are very sensitive to changes in the PSF structure, both over the field of view and as a function of time. The ability to accurately measure and characterize the shapes of faint, barely-resolved objects indicative of weak gravitational lensing, for example, depends on an intimate knowledge of the PSF and its variations.⁵ Crowded field time-series photometry⁶ and high-contrast imaging⁷ have also proven to be fields of study in which understanding how the PSF varies with time over the observed field of view is critical to the scientific result.

The primary source of PSF variations over the respective fields-of-view of the HST science instruments is a combination of defocus, coma, and astigmatism. These classical aberrations are present in practically every optical system due to design constraints and fabrication errors, and HST is no exception. Each of the aforementioned aberration will reduce the flux within the core of the PSF and redistribute that into the “wings” or “halo” surrounding the core, degrading the encircled energy (EE) within a small aperture. How that light is redistributed depends upon the aberration.

2.0.1. Spherical Aberration

The original HST prescription called for an f/24 Ritchey-Chretien telescope with a 2.4 m Primary Mirror ground with a conic constant of $\kappa = -1.0022985$. However, investigations after HST was placed into low-Earth orbit suggested that the actual conic constant of the HST PM was built to be closer to $\kappa = -1.0139$.⁸ As a result, all HST observations prior to the first Servicing Mission in December 1993 suffered from spherical aberration. The hallmark of such aberration is the lack of a crisp focus to the PSF, with a bright central core surrounded by a diffuse, generally symmetric halo. In the case of HST, features in the HST pupil also contributed to the structure of the halo,⁸ further complicating the PSF. Extended sources showed a distinct reduction in both resolution and contrast.

All instruments installed during and after the first Servicing Mission contain internal optics to correct for the spherical aberration present in HST’s Optical Telescope Assembly (OTA).

2.0.2. Defocus

Defocus is often apparent in wide-field imaging systems because the focal plane is usually a curved (non-planar) surface. The primary effect of defocus on the PSF is the symmetrical redistribution of flux from the PSF core into the adjacent diffraction rings, reducing contrast and sharpness. Small focus changes, however, do not significantly alter the width of the PSF core. Optically-induced defocus usually increases away from the center of the camera, but sometimes tilt or warping of the detector can create larger variations over the field (as in the case for the Advanced Camera for Surveys, see Sec. 2.2).

2.0.3. Coma

Coma is a third-order aberration that distorts the appearance of the PSF, skewing the core to one side and producing a classical V-shaped flaring that resembles a comet tail. While large amounts of coma may be readily apparent in well-sampled imaging systems,⁹ such an aberration would be much less apparent in a system that’s not critically-sampled. Even small amounts of coma can shift the PSF centroid by a significant fraction of a pixel, potentially impacting the precision with which an astrometric solution can be determined.

2.0.4. Astigmatism

Astigmatism is the result of an asymmetric focusing of the tangential and sagittal portions of an off-axis target’s PSF, elongating the PSF along one axis. The effects of astigmatism are strongly dependent on the system defocus, and angle of the major axis of an astigmatic PSF will change by 90° as the system moves through focus. Most observing systems are designed so as to minimize stigmatism at the camera’s optical center, with the result that PSFs at the center are generally symmetric. However, as one moves away from the optical axis, the PSF will tend to look more and more elongated.

Because of it’s Ritchey-Chretien design, HST trades third-order coma and spherical aberration for fifth-order coma, large-angle astigmatism, and significant field curvature. Thus, by design, HST shows significant astigmatism off its optical axis. Since the majority of HST’s scientific instruments “live” off-axis, each of these instruments are equipped with optics that correct for both the spherical aberration and the astigmatism present at that instrument’s position in the HST focal plane.

2.0.5. Geometric Distortion

Another optical artifact, geometric distortion, is not really a wavefront aberration but rather a sky-to-detector projection effect that can alter the scale over the field of view. Geometrical distortion in ACS, for example, skews the imaged PSF, slightly elongating the core in a manner that resembles astigmatism. Distortion is discussed in detail in other documents,^{10,11} and will not be explored further in this manuscript.

2.1. The Wide-Field and Planetary Camera 2

The Wide-Field and Planetary Camera 2 (WFPC2),¹² installed during the first HST Servicing Mission, is the only dedicated science instrument to occupy one of the four HST radial bays (the other three radial bays are occupied by the Fine Guidance Sensors). The WFPC2 field-of-view is centered on the HST optical axis. A pyramidal mirror in the HST focal plane splits the (aberrated) field onto four separate CCDs covering contiguous regions of the sky. The three Wide-Field Cameras (WFC) each cover a field-of-view of 75×75 arcseconds with a spatial sampling of $0.10''$ per pixel. The Planetary Camera (PC) covers a 34×34 arcsecond field with a spatial sampling of $0.046''$ per pixel. The three WFCs undersample the OTA’s point spread function by a factor of 4 at $\lambda = 5800\text{\AA}$ in order to provide an adequate field-of-view for studying galaxies, clusters of galaxies, etc.

Each of the four facets of the WFPC2 pyramid is a concave spherical surface. An image of the HST focal plane is relayed from each pyramid facet to a Cassegrain relay by an optical flat. An image of the HST primary mirror is formed at each of the secondary mirrors in the Cassegrain relays. These secondary mirrors are aspheric, and were designed to correct for the the spherical aberration from the HST primary mirror before forming a corrected image on the WFPC2 detectors. Each detector is housed in a cell that is sealed by an MgF_2 window that is figured to serve as a field flattener.

2.1.1. WFPC2 Field-Dependent PSF Variations

Field dependent variations due to the HST OTA as observed in WFPC2 are small, owing in large part to telescope’s Ritchey-Chretien design (which minimizes on-axis aberrations) and the instrument’s placement in the HST focal plane. However, the WFPC2 PSF does varies significantly with field position, a result of changes in the internal obscuration pattern due to the Cassegrain repeater optics described in Sec. 2.1. Each of the repeater secondary mirrors is supported by a set of support vanes. Since these structures are not located at a pupil, their silhouettes appear to shift relative to the HST OTA’s obscurations when projected into the exit pupil. At the edges of each WFPC2 detector, the PSF core is significantly elongated due to the large apparent shift between the telescope and repeater secondary positions. This makes small-aperture photometry or weak lensing studies extremely difficult to do in WFPC2. Even small offsets can alter the PSF enough to affect high-contrast programs that rely on a stable PSF (e.g, for reference star subtraction).

2.1.2. WFPC2 Charge Transfer Efficiency

The Charge Transfer Efficiency (CTE) of a Charge-Coupled Device (CCD) can be described as the efficiency with which photoelectrons are transferred from one pixel to an adjacent pixel during the shift operation required to read out the CCD. Unfortunately, this transfer is not 100% efficient, and some of the electrons are “lost” in traps in the silicon that comprises the CCD. During the readout process these traps capture charge as the image is shifted across the CCD towards the readout amplifier. The charge is released after a delay, but by that time the affected portion of the image has been clocked away from the trap, so the electron is released at some distance from its original position in the image. This process has the effect of producing tails on images, the relative brightness of which depends on the number of electrons originally present in the image.¹²

Unfortunately, the CTE for WFPC2 has increased with time, presumably a result of radiation damage to the detectors over the instrument’s lifetime. Recent work⁴ has similarly suggested a increase in the amount of Y-coma measured over the lifetime of the PC. The lack of a corresponding increase in X-coma has led to the suggestion that this measured Y-coma is actually a result of the degrading CTE, and may not be an optical effect. Work on this subject is on-going, and will be reported in future proceedings.

2.2. The Advanced Camera for Surveys

The Advanced Camera for Surveys (ACS)¹¹ is third-generation HST instrument, installed during Servicing Mission 3B. The ACS is comprised of three cameras using two imaging channels: one for the Wide Field Camera (WFC), and one shared by the High Resolution Camera (HRC) and the Solar Blind Channel (SBC). The WFC employs a mosaic of two 4096×2048 Scientific Imaging Technologies (SITe) CCDs with ~ 0.05 arcseconds per pixel spatial resolution and critical sampling at $11,600\text{\AA}$, resulting in a nominal field-of-view (FOV) of 202×202 arcseconds. The field center of the WFC is ~ 352.25 arcseconds away the HST optical axis.

The HRC detector is a 1024×1024 SITe CCD, with $\sim 0.028 \times 0.025$ arcseconds per pixel spatial resolution. The HRC is critical sampled at 6300\AA , giving this detector a nominal 29×26 arcsecond FOV.

The SBC detector is a solar-blind CsI microchannel plate (MCP) with Multi-Anode Microchannel Array (MAMA) readout. It has 1024×1024 pixels, each providing a spatial resolution of $\sim 0.034 \times 0.030$ arcseconds. Together, this array yields a nominal FOV of 35×31 arcseconds. The SBC is a UV-optimized instrument with a spectral response range from 1150\AA to 1700\AA . The SBC and HRC share the same position in the HST focal plane (~ 515.33 arcseconds from the HST optical axis), and are selectable by means of a fold flat mirror. Since the SBC is not routinely used for the science outlined above, we will not discuss its behavior in detail.

2.2.1. ACS Geometric Distortion

Geometric distortions produce a significant impact on the shape of the PSF in all three of the ACS channels. The distortion owes primarily to the tilt of each focal surface to the chief ray at the position of the ACS apertures in the HST focal plane (focal plane tilts of 20° in the WFC and 31° in both the HRC and SBC). The linear, field-independent approximation for the WFC yields a difference in plate scale of about 8% between the two diagonals of the field and about a 16.5% difference in scale between orthogonal directions rotated about 20° from the aperture edges in the HRC and SBC. Field-dependent distortions, measured as actual vs. predicted distances from field center, amount to about 2% peak in the WFC and about 1% in the HRC and SBC. The distortions render the pixels trapezoidal in shape as projected on the sky, with the projected area of those pixels varying by about 19% in the WFC field and 3.5% in the HRC and SBC^{9,11} fields respectively.

2.2.2. ACS Field-Dependent PSF Variations

Residual aberration levels at the center of field in each of the ACS imaging channels are low ($\sim 1/20^{\text{th}}$ wave rms in WFC and $\sim 1/30^{\text{th}}$ wave rms in the HRC at $\lambda = 0.55\mu\text{m}$), with both coma and astigmatism minimized at these positions. The ACS PSF varies far less over the field than the WFPC2 PSF, which suffers from the variable obscuration pattern described in Sec 2.1.1. In ACS, PSF variations over the field are generally a result of changes in aberrations and charge diffusion. Increased astigmatism at the extreme corners of the WFC field slightly elongates the PSF core. If temperature-induced variations in the OTA (“breathing”, see Sec. 3) cause the system to pass through nominal focus, the axis of elongation of the astigmatic PSF core will rotate by 90° . Such variations may affect ellipticity measurements of small galaxies with bright cores at the field edges.

As noted in previous work,¹³ much of the field-dependent blurring of the PSFs in the WFC can be attributed to variations in charge diffusion over the WFC CCDs. This variation is caused when electrons generated by interactions between photons and the CCD’s photosensitive epitaxial layer “wander” from the nearest pixel to an adjacent pixel. Since the WFC CCDs are backside-illuminated devices, photons that are absorbed closer to the illuminated surface (e.g, short-wavelength photons) show the greatest propensity for charge diffusion.

The sensitivity of backside-illuminated CCDs to short-wavelength photons can be enhanced by “thinning” the CCD’s epitaxial layer through photochemical etching. An unfortunate by-product of this processing is a variation in the thickness of the remaining epitaxial layer, which in turn can create a field-dependent variation in charge diffusion. Measurements of the effect of charge diffusion on the PSF core over the WFC field shows a strong correlation¹³ with CCD thickness variation measurements derived from flat field data.*

2.3. NICMOS

NICMOS, the Near Infrared Camera and Multi-Object Spectrometer,¹⁵ is an HST axial instrument containing three cameras designed for simultaneous operation. The NICMOS optics offer three adjacent, but not spatially contiguous fields-of-view of different image scales. The instrument covers the wavelength range from $\lambda = 0.8$ to $2.5\mu m$, with its highest sensitivities between $\lambda = 1.1$ and $\sim 2.0\mu m$.

The NICMOS fore-optics assembly is designed to correct the spherically aberrated HST beam. Input from the HST OTA first reflects off the Pupil Alignment Mechanism (PAM), an adjustable mirror in the NICMOS optical train that can be used to make small corrections to the NICMOS focus. PAM adjustments also serve to position the beam onto a re-imaging mirror, which focuses an image of the OTA pupil onto a Field-Offset Mechanism (FOM). The FOM houses the optics that correct the beam for spherical aberration from the HST OTA. From the FOM, the corrected beam is then directed into each of the three NICMOS imagers (NIC1, NIC2, and NIC3).

NICMOS provides full Nyquist sampling beyond $\lambda = 1.0\mu m$ and $\lambda \sim 1.7\mu m$ in NIC1 and NIC2, respectively. In contrast, NIC3 has the lowest spatial resolution of the three NICMOS imagers, but covers the largest FOV.

While the PAM and the FOM were designed to allow for adjustment of the NICMOS focus and alignment positions through the instrument’s life, thermal stresses suffered by the NICMOS dewar early in the instrument’s life have pushed the nominal focus for the NIC3 camera beyond the available range of the PAM (though NIC1 and NIC2 are nearly parfocal, with nominal focus within the PAM adjustment range). Observations with NIC3 typically show a loss of peak flux of $\sim 20\%$. However, because NIC3 undersampled the HST PSF by design, the loss of performance with the camera out-of-focus was not seen as critical to the instrument’s operations. As such, NIC3 continues to be offered as a selectable mode of NICMOS imaging.

Each NICMOS camera has a cold mask located at the entrance to the dewar that is designed to block thermal emission from the OTA pupil obstructions. As a result of the thermal stress experienced by the NICMOS dewar, the cold masks for each imaging channel have shifted, in some cases by as much as 12% of the beam diameter. Because of this, the point source diffraction pattern in NICMOS images is not symmetric, with elliptical diffraction rings and asymmetric distributions of light and dark bands present the diffraction spikes. Over time, these cold masks have shifted in position, further complicating NICMOS image analyses. In addition, a short temporal variation in the cold mask position (“wobble”) of order 0.5% of the beam diameter continue to be observed over orbital timescales.

Coma and astigmatism in the NICMOS cameras are generally small, with the wavefront error typically less than $0.05\mu m$. The PSF does show a field dependence in all NICMOS cameras. Preliminary data indicate this effect is small, with only a $\sim 6\%$ variation the PSF FWHM across the field.

Because the wavelength sensitivity of NICMOS is in the near-Infrared, its PSFs show increasingly less dependence on the optical aberrations and zonal mirror polishing errors⁸ (though the NICMOS PSF is still fairly sensitive to these errors in the J-band). However, the NICMOS PSF does suffer from the temporal variations induced by the HST “breathing” (see Sec. 3) in addition to the cold mask variations described above. A comprehensive review of the NICMOS PSF has been presented in other documents,¹⁶ and will not be discussed in detail here.

*The thickness of the ACS CCDs varies between 12.6 and $17.0\mu m$ in the WFC and 12.5 and $16.0\mu m$ in the HRC.¹⁴

3. EFFECTS OF OTA VARIATIONS ON THE OBSERVED PSF

Unlike ground-based observatories, the HST PSF is not affected by atmospheric turbulence, so smaller-amplitude wavefront variations caused by optical and mechanical instabilities create the most noticeable changes in the PSF. Primary among these are thermally-induced OTA focus changes that alter the distribution of light between the wings and core of the PSF. In the presence of other aberrations – most notably astigmatism – the symmetrical nature of the PSF can change as the focus changes.⁷ For most HST pointings, the HST FOV will typically be occulted by the Earth during some portion of the orbit, the exception being for those pointings where the HST boresight is directed towards either of its continuous viewing zones (CVZs) near its orbital poles. During Earth occultation, the interior of telescope absorbs thermal emission from the bright limb of the planet, which causes an expansion of the OTA truss.⁴ After the occultation the telescope will thermally relax and the OTA truss will contract. This cycle is repeated every orbit (hence the term “breathing”), though the amplitude of this expansion and contraction will depend on the current boresight pointing as well as the pointing history of the previous few orbits. Typically, the separation between the Primary and Secondary Mirrors changes by 3 to 5 μm , resulting in focus changes between 1/27th and 1/16th wave RMS at $\lambda = 0.5\mu\text{m}$ in the HST focal plane. However, separations as high as 7 to 10 μm have been detected under extreme circumstances.

3.1. PSF FWHM and Ellipticity

HST was originally designed to use three rate-sensing gyroscopes to provide fine pointing control of the Observatory during science observations. In order to conserve the lifetime of these gyroscopes, the HST Project made the decision to turn off one of the functioning gyros and to upload a new attitude control system that functions with only two gyros in the fine pointing control loop. The Two-Gyro Science Mode was initiated on August 28, 2005.

As part of the Two-Gyro Science Mode Orbital Verification (TGSMOV), a series of observations with the ACS point spread function (PSF) shape and stability tests were conducted. These tests consisted of multiple exposures of three stellar clusters observed with the HRC in the F555W filter. Observing sequences of 10, 100, and 500 second exposures were used to check for dependencies of the PSF shape on exposure duration and timing within orbits. For each image, the FWHM of the PSF for stars with $S/N > 10$ was calculated by fitting Gaussian profiles to the stellar light profiles. This typically resulted in hundreds of measurements per image, which were then averaged to produce a mean PSF width for each image with an uncertainty of $\sim 0.05 - 0.15$ pixels, depending on the number and brightnesses of the stars used in the mean. A broadening of the measured PSF FWHM was noted from these data as a function of time within the orbit, suggesting a dependence that is likely due to the focus changes associated with the breathing of the OTA.

Fig. 1 shows a comparison of these FWHM measurements for a portion of the Two-Gyro Servicing Mission Orbital Verification (TGSMOV) test data and a model of the expected changes caused by the breathing cycle. The typical PSF width change shown in this figure are ~ 0.1 pixel. The magnitude of this effect and the amplitude of the breathing model for any given pointing will depend upon the thermal stability of the Observatory at that position.

3.2. Phase Retrieval

Many of the aberrations observed in the HST PSF associated with OTA and science instruments are difficult to distinguish without high signal-to-noise point source observations and specialized fitting code. Much of our knowledge of this subject comes from specialized calibration programs to monitor the HST PSF and analysis of those PSFs using parametric (model-fitting) phase retrieval. Utilizing mirror maps based on previously determined mid-frequency wavefront errors,⁸ the technique iteratively generates model PSFs and compares them with the observed data. The wavefront error is characterized by the series of Mahajan Zernike polynomials¹⁷ modified for the 0.33 obscuration applicable to HST. Our PSF fits normally involve focus, wavefront tilt, astigmatism, and coma. The coefficients for the higher order Zernike terms contribute little and are fixed at established values or taken as zero. The definitions of the aberration polynomials of interest are given in a companion paper.⁴ A detailed discussion of phase retrieval techniques and wavefront aberrations for HST is given elsewhere.⁸

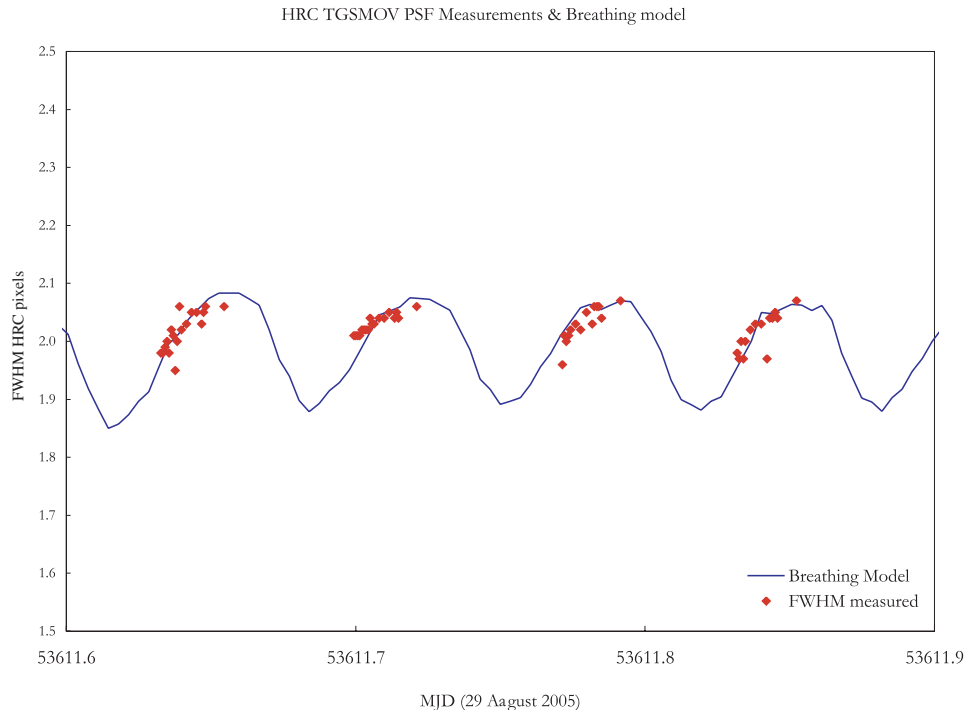


Figure 1. PSF Full-Width at Half-Maximum (FWHM) measurements in the ACS/HRC as part of the Two-Gyro Servicing Mission Orbital Verification (TGSMOV) testing. The broadening of the observed PSF over time is consistent with variations expected due to the “breathing” of the HST OTA during a typical orbit. The typical change in the PSF FWHM in this figure is ~ 0.1 pixels.

4. SCIENCE IMPACT OF OBSERVED PSF VARIATIONS

We show how variations in these quantities over the timescales observed may impact the photometric and astrometric precision required of many current HST programs, as well as the characterization of barely-resolved objects.

4.1. Observed and Modeled PSF Ellipticities in WFC

It is well known that the morphology of the ACS PSF in both WFC and HRC exhibits appreciable field dependence.¹³ However, the understanding of how that PSF morphology varies over time and as a function of e.g. focus has not been well understood. Understanding the ACS PSF and the factors that affect it has become increasingly important as science observations in fields such as weak lensing and circumstellar environments continue to push the limits of what is observable.

The analysis of the PSF ellipticity in ACS/WFC provides direct evidence of both the field variations of the PSF and their dependence on time. The ellipticity of the PSF is of special interest because it is the property that most directly affects weak lensing measurements, which are among the ACS science observations that are most sensitive to systematic effects - the typical signature of cosmic shear translates into a 1 % distortion of the shape of faint galaxies, while the ellipticity of the PSF varies by several percent. Several methods have been developed to remove PSF effects from galaxy shape measurements;^{18–21} however, their success depends critically on an accurate and reliable characterization of the PSF itself *at the time the images were taken*.⁵ Note also that the definition of PSF ellipticity is very sensitive to the details of the procedure used to measure it; even similar methods can yield significantly different measurements depending on the exact choice of parameters.

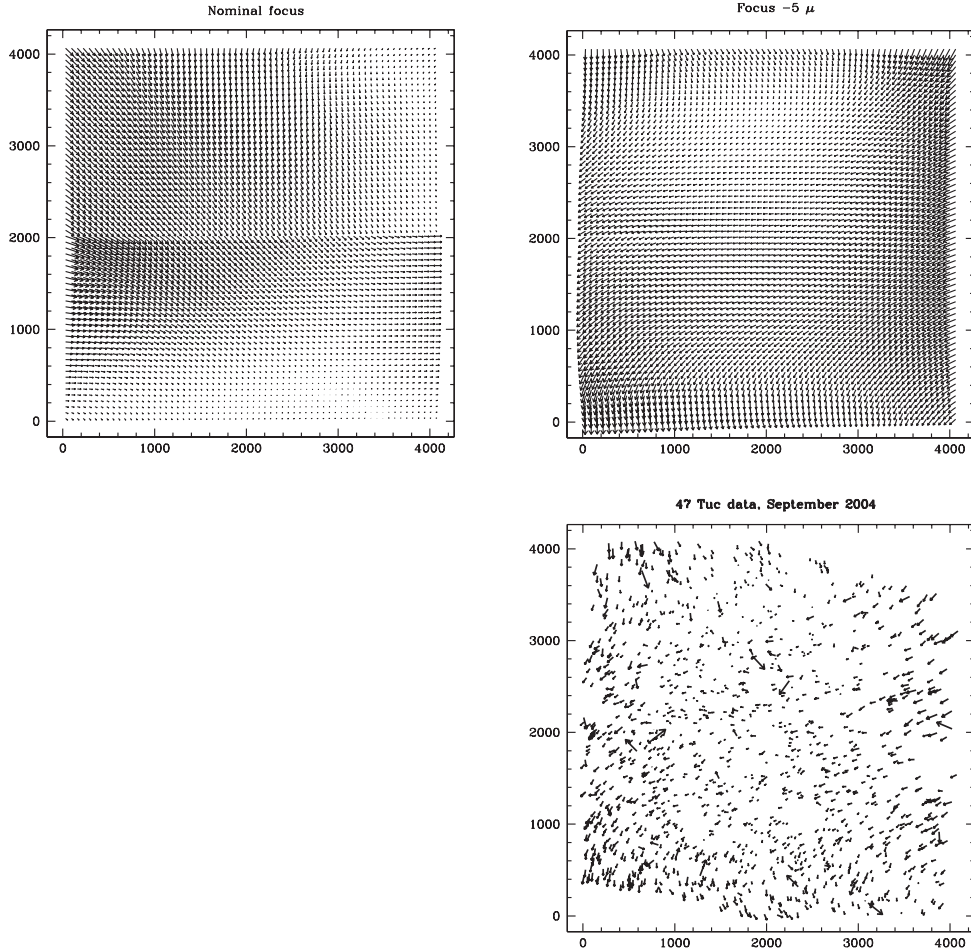


Figure 2. PSF ellipticities in the ACS/WFC measured from Tiny Tim PSF models. At top-left: ellipticities measured from models at nominal focus. At top-right: ellipticities measured from models at $\sim -5\mu\text{m}$ of SM despace. At bottom-right: PSF ellipticities of stellar sources in 47 *Tuc* observed in the ACS/WFC with *F814W* while *HST* was known to be in a negative focus state of $\sim -5\mu\text{m}$

For the purpose of characterizing the PSF ellipticity in stellar images, we use a simple definition based on the second-order moments of the PSF weighted with a circular Gaussian. The use of a weighting function improves the quality of the measurement by suppressing the noise in the tail of the PSF and by providing a stable measuring window; note that the second-order moment of an unweighted PSF is not well-defined, as the relevant integral diverges logarithmically at large radii even for a perfect PSF. Empirically, we find that the smallest Gaussian scale that can be used to measure PSF properties in ACS/WFC is 1 pixel; smaller scales yield results that depend strongly on the subpixel centering of the PSF. Thus the ellipticities quoted here are based on a Gaussian weight function with scale 1 pixel. It is also important to note that the ellipticities quoted are in the original pixel frame, thus they are affected by the geometric distortion of ACS/WFC. It is possible to work either in original pixels or in rectified coordinates, e.g., by using the images produced by the HST pipeline using the drizzle procedure. The latter remove, to some extent, the geometric distortion but add other artifacts that can depend on the relative position of pixel centers in the original and rectified images. For this reason, we prefer to work in original pixels.

Figures along the top in Fig. 2 show the ellipticity pattern in WFC obtained from measurements of TinyTim

model PSFs. These patterns are due to the combination of the geometric distortion of ACS/WFC with variations due to the camera optics and to variations in the chip thickness.⁷ The top-left figure refers to the camera at nominal focus, while the top-right figure shows the substantially different ellipticity pattern when the secondary mirror is displaced 5 microns closer to the primary mirror than nominal. The geometric distortion is essentially identical in the two cases, so the variation of the PSF ellipticity pattern is entirely due to defocus. The figure at bottom-right shows an actual measurement of an image of a star-rich field, taken in September 2004 when the secondary mirror offset from best focus was measured to be close to $\sim -5\mu m$; the close similarity between the measured ellipticity pattern and the prediction for the same focus position clearly demonstrates that the TinyTim model captures the essence of the change in PSF.

As shown clearly by others,^{5,22} careful consideration of the focus position of HST will be a crucial component of the analysis of weak lensing observations. It is yet to be determined whether other aberrations, such as coma and astigmatism, can similarly affect weak lensing observations at a level significant in comparison with the expected signal and the intrinsic measurement noise.

4.2. Modeled Ellipticities in HRC

Using Tiny Tim, we generated model PSFs with the F555W filter on a 16×16 grid of positions across the HRC field. We examined the variation of the PSF ellipticity in the original pixel frame as a function of focus (holding coma and astigmatism constant), and as a function of coma and of astigmatism at nominal focus.

Fig.3 illustrates the change in ellipticities over typical ranges of HST focus: from a positive focus state ($+2.75\mu m$, top-left), to nominal focus (top-right), to $-2.75\mu m$ (bottom-left) and $-5\mu m$ (bottom-right) of Secondary Mirror despace (relative to the Primary Mirror). It is clear that as with WFC, changes in focus at the HRC induce a measurable effect on ellipticity, with the most notable change seen from the positive focus state to nominal focus. We presume the observed changes are due to astigmatic variations in the PSF due to the combined effects of the HST OTA and the ACS optics. However, these effects are much less pronounced than in the WFC, and would be difficult to characterize directly from science images. Work is on-going to determine the sources of the coma and astigmatism variations described in a companion paper⁴ (e.g. are they a result of motions of the HST OTA, or of motions of optics within the ACS itself?).

4.3. Photometry

Science currently expected to be performed with the Cosmic Origins Spectrograph and Wide Field Camera 3 (COS and WFC3 respectively, expected to be installed as part of HST Servicing Mission 4) will most likely be sensitive to a varying PSF. The impact of PSF variations could be estimated and assessed in advance of the installation of these instruments. In the time prior to Servicing Mission 1, the dilated, spherically aberrated PSF, combined with a number of small apertures, made throughput quite sensitive to orbital breathing. In the current epoch, observing programs that depend sensitively on a stable or well-modeled PSF, are drivers for a better understanding of the sources and timescales of observed PSF variations. Previous work²³ has shown that the SM despace variations of a few microns typical of breathing alter photometry for the different WFPC2 cameras by as much as 10% for a photometric aperture of radius 1 pixel, and a few percent for a common aperture of radius 2 pixels. These results are notably worse than the general accuracy goal of 1% photometry for HST. Some authors have discussed actively tracking PSF changes in time⁶ and using the knowledge of these changes in one's data analysis. Accounting for PSF changes was critical to the science goals of week-long observing campaigns of 47 Tucana (PI: Gilliland, proposals 8267 & 9750) aimed at detecting extrasolar planet transits with photometric precisions near the theoretical limit (0.3% WFPC2, 0.2% ACS). Addressing the rapidly changing PSF for these crowded-field photometry programs provided the greatest challenges in terms of software development and execution time.

4.4. High dynamic range imaging

Over the years, observers have dedicated a lot of time and effort to using HST as a high-contrast imaging system, in part due to its relative stability compared with ground-based platforms. Though not specifically designed as a high-contrast imaging platform, the use of coronagraphs to suppress stellar diffraction patterns and reference PSF subtraction have enabled contrast improvements of a factor of 1000 over direct imaging alone.

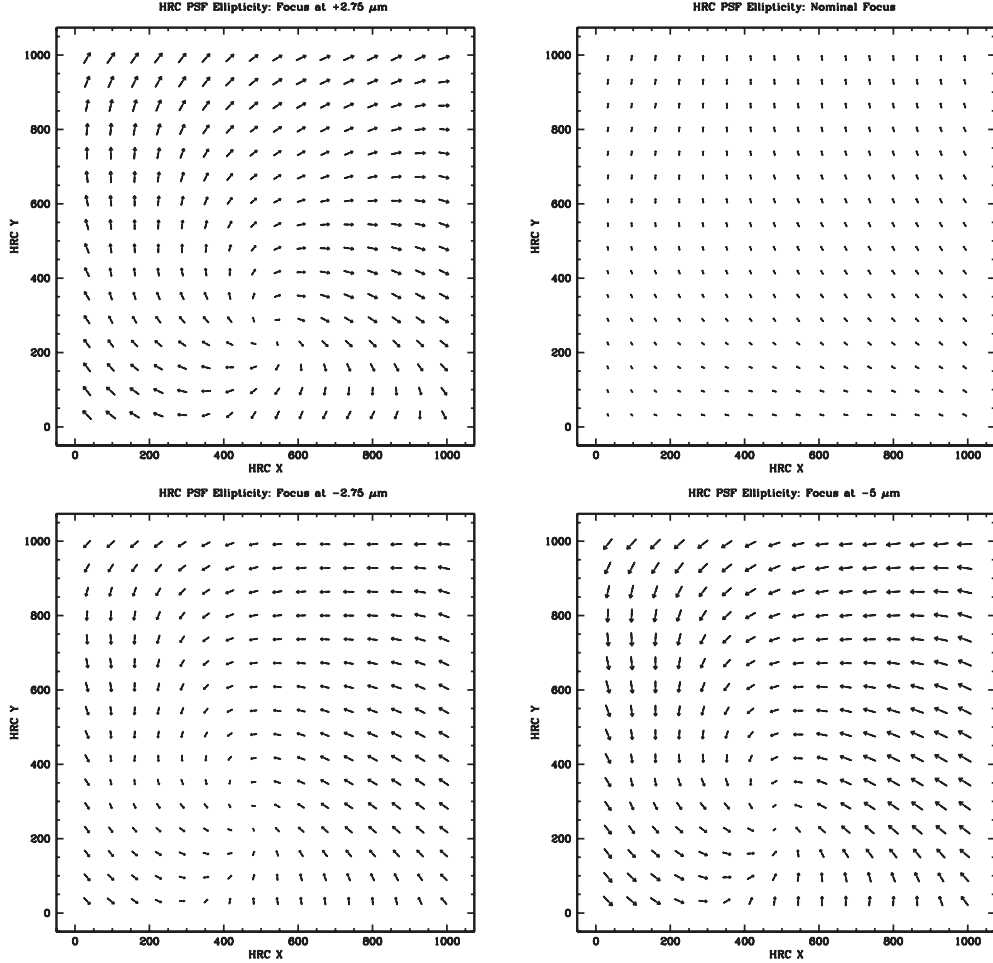


Figure 3. Measured changes in PSF ellipticity in the HRC original pixel frame from Tiny Tim models at HST Secondary Mirror despace positions of $+2.75\mu\text{m}$ (top-left), nominal focus (top-right), $-2.75\mu\text{m}$ (bottom-left) and $-5\mu\text{m}$ (bottom-right). Here, the length of each vector is given by $5e$, where e is the measured ellipticity of the PSF at that position. These simulations assumed nominal values for OTA coma and astigmatism at the position of the ACS High Resolution Camera. Apparent changes in the magnitude and direction of ellipticity in the original pixel frame are typically small compared with those noted from the WFC simulations.

Previous work by the authors and others^{13, 16, 24} have elucidated the challenges faced by high-contrast imaging with HST, and we refer the reader to those references for more details.

5. SUMMARY

While HST has proven to be a stable platform for astronomical observations, especially when compared with ground-based optical observatories, certain high-precision observations with HST continued to be challenged by small-amplitude wavefront variations caused by optical and mechanical instabilities. Thermally-induced focus changes have been shown to be the primary cause of many of the variations seen in the HST PSF, though other aberrations are also present. How these other aberrations – notably coma, astigmatism, and the field-dependent morphology of the PSF in the ACS WFC and HRC – interact with overall OTA aberrations is just now being understood. While these aberrations have been shown to exhibit behavior on orbital and longer timescales, the causes of these variations are not yet well-understood. Though the use of phase retrieval can precisely quantify these variations, more familiar—though less sensitive—“real world” characterizations of the observed PSF (e.g. encircled energy, FWHM, and ellipticity) are far less sensitive to the range of coma and astigmatism observed than to focus. Understanding the state of the HST focus at the time of one’s observations is necessary to achieve the photometric and astrometric precisions required of many current HST programs,^{6, 23} and to accurately describe the morphologies of barely resolved objects.

We hope that ongoing work to characterize and model the HST PSF will enable HST observers achieve the full science capabilities of the observatory, both with the current generation of instruments and with the future generation of HST instruments.

ACKNOWLEDGMENTS

The authors would like to thank Jay Anderson and Jason Rhodes for their discussions on the distortion solution of WFPC2 and ACS and on modeling the time-dependent ACS PSF respectively. We would also like to thank the HST Mission Office at the Space Telescope Science Institute for their support in the analysis and characterization of the HST PSF.

REFERENCES

1. T. R. Lauer, S. M. Faber, R. C. Lynds, W. A. Baum, S. P. Ewald, E. J. Groth, J. J. Hester, J. A. Holtzman, J. Kristian, R. M. Light, E. J. O’Neil, D. P. Schneider, E. J. Shaya, and J. A. Westphal, “Planetary Camera observations of the M87 stellar cusp,” *Astronomical Journal* **103**, pp. 703–710, Mar. 1992.
2. C. R. O’dell, Z. Wen, and X. Hu, “Discovery of new objects in the Orion nebula on HST images - Shocks, compact sources, and protoplanetary disks,” *Astrophysical Journal* **410**, pp. 696–700, June 1993.
3. C. J. Grillmair, S. M. Faber, T. R. Lauer, W. A. Baum, R. C. Lynds, E. J. O’Neil, and E. J. Shaya, “The nuclear regions of NGC 3311 and NGC 7768 imaged with the Hubble Space Telescope Planetary Camera,” *Astronomical Journal* **108**, pp. 102–110, July 1994.
4. M. D. Lallo, R. B. Makidon, S. Casertano, and J. E. Krist, “The Temporal Optical Behavior of HST: Focus, Coma, & Astigmatism History,” in *Observatory Operations: Strategies, Processes, and Systems. Edited by Silva, David R. Doxsey, Rodger E. Proceedings of the SPIE, Volume 6270, this volume.*, C. Cunningham and J. Oschmann, eds., 2006.
5. J. Rhodes, R. Massey, J. Albert, J. E. Taylor, A. M. Koekemoer, and A. Leauthaud, “Modeling and Correcting the Time-Dependent ACS PSF,” in *The 2005 HST Calibration Workshop: Hubble After the Transition to Two-Gyro Mode*, A. M. Koekemoer, P. Goudfroiij, L. L. Dressel, ed., *HST Calibration Workshop*, pp. 21–30, 2006.
6. R. L. Gilliland, T. M. Brown, P. Guhathakurta, A. Sarajedini, E. F. Milone, M. D. Albrow, N. R. Baliber, H. Bruntt, A. Burrows, D. Charbonneau, P. Choi, W. D. Cochran, P. D. Edmonds, S. Frandsen, J. H. Howell, D. N. C. Lin, G. W. Marcy, M. Mayor, D. Naef, S. Sigurdsson, C. R. Stagg, D. A. Vandenberg, S. S. Vogt, and M. D. Williams, “A Lack of Planets in 47 Tucanae from a Hubble Space Telescope Search,” *Astrophysical Journal* **545**, pp. L47–L51, Dec. 2000.

7. J. E. Krist, "High-contrast imaging with the Hubble Space Telescope: performance and lessons learned," in *Microwave and Terahertz Photonics. Edited by Stohr, Andreas; Jager, Dieter; Iezekiel, Stavros. Proceedings of the SPIE, Volume 5487, pp. 1284-1295 (2004).*, J. C. Mather, ed., pp. 1284–1295, Oct. 2004.
8. J. E. Krist and C. J. Burrows, "Phase-retrieval analysis of pre-and post-repair Hubble Space Telescope images," *Applied Optics* **34**, pp. 4951–4964, Aug. 1995.
9. G. F. Hartig, J. E. Krist, A. R. Martel, H. C. Ford, and G. D. Illingworth, "On-orbit alignment and imaging performance of the HST advanced camera for surveys," in *Future EUV/UV and Visible Space Astrophysics Missions and Instrumentation. Edited by J. Chris Blades, Oswald H. W. Siegmund. Proceedings of the SPIE, Volume 4854, pp. 532-543 (2003).*, J. C. Blades and O. H. W. Siegmund, eds., pp. 532–543, Feb. 2003.
10. J. Anderson and I. R. King, "PSFs, Photometry, and Astrometry for the ACS/WFC," *Instrument Science Report (ACS 2006-01; Baltimore: STScI)*.
11. S. Gonzaga et al., *ACS Instrument Handbook, Version 6.0*, (Baltimore: STScI), 2005.
12. I. Heyer and J. Biretta, *WFPC2 Instrument Handbook, Version 9.0*, (Baltimore: STScI), 2004.
13. J. E. Krist, "ACS WFC & HRC field-dependent PSF variations due to optical and charge diffusion effects," *Instrument Science Report (ACS 2003-06; Baltimore: STScI)*.
14. J. Walsh, W. Freudling, N. Pirzkal, and A. Pasquali, "Modelling the fringing of the ACS WFC and HRC chips," *Instrument Science Report (ACS 03-12; Baltimore: STScI)*.
15. A. e. a. Schults, *NICMOS Instrument Handbook, Version 8.0*, (Baltimore: STScI), 2005.
16. J. E. Krist, D. A. Golimowski, D. J. Schroeder, and T. J. Henry, "Characterization and Subtraction of Well-Exposed HST/NICMOS Camera 2 Point-Spread Functions for a Survey of Very Low Mass Companions to Nearby Stars," *Pub. Astron. Society of the Pacific* **110**, pp. 1046–1058, Sept. 1998.
17. V. N. Mahajan, "Zernike annular polynomials for imaging systems with annular pupils," *Journal of the Optical Society of America A* **1**, pp. 685–+, June 1984.
18. J. Rhodes, A. Refregier, and E. J. Groth, "Weak Lensing Measurements: A Revisited Method and Application to Hubble Space Telescope Images," *Astrophysical Journal* **536**, pp. 79–100, June 2000.
19. G. M. Bernstein and M. Jarvis, "Shapes and Shears, Stars and Smears: Optimal Measurements for Weak Lensing," *Astronomical Journal* **123**, pp. 583–618, Feb. 2002.
20. S. Casertano, K. U. Ratnatunga, and R. E. Griffiths, "Cosmic Gravitational Shear from the Hubble Space Telescope Medium Deep Survey," *Astrophysical Journal* **598**, pp. L71–L74, Dec. 2003.
21. C. Heymans, M. L. Brown, M. Barden, J. A. R. Caldwell, K. Jahnke, C. Y. Peng, H.-W. Rix, A. Taylor, S. V. W. Beckwith, E. F. Bell, A. Borch, B. Häußler, S. Jogee, D. H. McIntosh, K. Meisenheimer, S. F. Sánchez, R. Somerville, L. Wisotzki, and C. Wolf, "Cosmological weak lensing with the HST GEMS survey," *Monthly Notices of the Royal Astronomical Society* **361**, pp. 160–176, July 2005.
22. Y. Park, S. Casertano, and H. C. Ferguson, "Optimal Galaxy Shape Measurements for Weak Lensing Applications Using the Hubble Space Telescope Advanced Camera for Surveys," *Astrophysical Journal* **600**, pp. L159–L162, Jan. 2004.
23. A. Suchkov and S. Casertano, "Impact of Focus Drift on Aperture Photometry," *Instrument Science Report (WFPC2 1997-01; Baltimore: STScI)*.
24. G. Schneider, E. E. Becklin, B. A. Smith, A. J. Weinberger, M. Silverstone, and D. C. Hines, "NICMOS Coronagraphic Observations of 55 Cancri," *Astronomical Journal* **121**, pp. 525–537, Jan. 2001.